buildings

MDPI

Article

Study on the Influence of Wind Fairing Parameters on the Aerodynamic Performance of Long-Span Double-Deck Steel Truss Suspension Bridge

Yang Yang [1], Long Li [1], Gang Yao [1,*], Bo Wu [2], Dawu Wang [3], Hui Yu [3] and Hao Qu [3]

[1] School of Civil Engineering, Chongqing University, Chongqing 400045, China; 20121601009@cqu.edu.cn (Y.Y.); 202216021032@stu.cqu.edu.cn (L.L.)
[2] School of Civil Engineering, Chongqing Jiaotong University, Chongqing 400074, China; bo.wu@cqjtu.edu.cn
[3] Chongqing Railway Group Co., Ltd., Chongqing 400015, China; 15023482432@163.com (D.W.); 15310239541@163.com (H.Y.); 15859073223@163.com (H.Q.)
* Correspondence: yaogang@cqu.edu.cn; Tel.: +86-13608361176

Abstract: A long-span double-deck steel truss suspension bridge is easy to produce vortex-induced vibration (VIV) at low air velocity, which affects bridge service life. Additional aerodynamic measures play a role in suppressing VIV by changing the aerodynamic shape, which is a common control method. As the main aerodynamic measure to suppress the VIV response, wind fairing is widely used in engineering practice. In order to obtain the optimal additional position and shape parameters of the fairing, Huangjuetuo Yangtze River Bridge is the research target. Through the combination of a wind tunnel test and numerical simulation, the VIV response of the original and fairing section is studied. Based on data analysis, it is revealed that these additional fairings to the upper chord can significantly reduce the VIV response. When the shape parameters of the fairing are h/D = 1/4 and l/D = 1, the VIV inhibition efficiency is the highest, which can reach 65.51%. By analyzing the flow distribution, it can be seen that VIV is caused mainly by vortex separation in the upper bridge board area. Although this wind fairing does not change the original vortex shedding forms, it changes the first separation point and movement direction of the airflow, making the vortex scale generated by the airflow smaller and the vorticity lower, thus effectively suppressing VIV.

Keywords: double-deck steel truss girder; aerodynamic performance; wind fairing; wind tunnel test; numerical simulation

check for updates

Citation: Yang, Y.; Li, L.; Yao, G.; Wu, B.; Wang, D.; Yu, H.; Qu, H. Study on the Influence of Wind Fairing Parameters on the Aerodynamic Performance of Long-Span Double-Deck Steel Truss Suspension Bridge. *Buildings* **2024**, *14*, 2255. https://doi.org/10.3390/buildings14072255

Academic Editor: Francesco Ricciardelli

Received: 13 June 2024
Revised: 12 July 2024
Accepted: 19 July 2024
Published: 22 July 2024

Copyright: © 2024 by the authors. Licensee MDPI, Basel, Switzerland. This article is an open access article distributed under the terms and conditions of the Creative Commons Attribution (CC BY) license (https://creativecommons.org/licenses/by/4.0/).

1. Introduction

Long-span bridges' modal frequency is always low, and vortex shedding is easy to occur when gas flows around the surface of the main girder, resulting in VIV. VIV has a limiting nature, although it cannot cause serious consequences such as bridge collapse caused by a divergent flutter of the bridge [1,2]. However, VIV has the characteristics of a low starting wind speed, large amplitude response and high frequency, which can easily cause the fatigue failure of a bridge's structure and affect structural safety. Also, a large VIV can easily cause social panic [3]. For example, China's Xihoumen Bridge [4] and Humen Bridge [5], Denmark's Great Belt Bridge [6], and Canada's Lions' Gate Bridge [7] all have VIV phenomena, so it is necessary to conduct special research on the VIV of long-span bridges.

The double-deck steel truss girder is a common girder form of a long-span suspension bridge, which can not only save line resources but also has excellent traffic capacity [8,9]. Studies have shown that when wind stream flows through a bridge's cross-section, it will generate obvious vortex generation, merging and shedding, resulting in periodic aerodynamic force [10–13]. Therefore, compared with the general single-deck main girder form, the aerodynamic shape of the more complex double-deck steel truss girder section

has a greater hidden danger of VIV [14]. Right now, studies on the VIV of long-span double-deck steel truss suspension bridges have been comparatively scarce, but the number of long-span bridges with double-layer deck truss girders as the main girder is increasing, and the problem of VIV is also becoming increasingly prominent [15,16]. Therefore, explorations on double-deck steel truss suspension bridge VIV should be given more attention.

A wind fairing is an additional aerodynamic measure widely used in bridge engineering. This additional aerodynamic measure is a kind of bridge VIV control method. Its principle is to change the aerodynamic shape by adding an additional structure so as to improve aerodynamic performance. Bai et al. [17] studied the inhibition effect of the angle and eccentric position of a fairing on the VIV of a π-type composite girder. Regarding a small-size fairing, the results show that its VIV inhibition effectiveness is better than that of a large-size fairing. Li et al. [18] explored how impact affects the fairing angle on the VIV performance of a streamlined trapezoidal box girder by numerical simulation. According to the simulation's outcome, changing the fairing angle can significantly affect VIV performance, and the maximum amplitude of VIV decreases with a decrease in the fairing angle.

In the existing research, more attention has been paid to the impact of fairings on the aerodynamic characteristics of a box girder as well as a π-girder, and many valuable conclusions have been obtained. However, there are relatively few studies on the optimization of the fairing parameters of long-span double-deck steel truss suspension bridges, and most of them only consider the influence of $\pm 3^\circ$ and 0° conventional wind attack angles, and the case of a large $\pm 5^\circ$ angle is rarely considered. Due to the large differences in the structural system, section form and dynamic performance of an actual long-span double-deck truss bridge, it is necessary to carry out a wind tunnel test and numerical simulation research when there is a big difference between the bridge terrain and the bridge structure system. In order to effectively suppress VIV, Huangjuetuo Yangtze River Bridge is chosen as the research target, and we carry out a wind tunnel test and numerical simulation to test aerodynamic performance under different fairing parameters at 0°, $\pm 3^\circ$ and $\pm 5^\circ$ so as to obtain the optimal aerodynamic optimization measures and the vibration inhibition mechanism of the fairing. The research results can provide an effective reference for the design of the same type of bridge in the future.

2. Implementation of Vortex-Induced Vibration

2.1. Parameters of Wind Fairing

In order to find out the optimal aerodynamic shape of a fairing section and analyze how impact affects the aerodynamic performance of a double-deck steel truss bridge, a wind fairing is studied and analyzed according to different layout positions and shape parameters. Firstly, the fairing is set at different positions, and the optimal fairing arrangement position is obtained through an performance evaluation index. Then, based on this, different shapes of the fairing are designed, and the optimal fairing parameters are obtained by comparing them with each other. There are six working conditions of C1~C6 designed according to the position of the fairing, as shown in Figure 1, which are an upper chord wind fairing, web rod wind fairing, lower chord wind fairing, upper chord wind fairing + lower chord wind fairing, upper chord wind fairing + web rod wind fairing, and web rod wind fairing + lower chord wind fairing.

When setting the shape parameters of the fairing, the height, D, of the truss section is taken as the quantitative variable, and the horizontal size, l, of fairing and the relative height, h, of the fairing are taken as the variables. A total of nine working conditions of F1~F9 are set, in which the h/D value is 3/4, 1/2, and 1/4, and the l/D value is 1/2, 2/3, and 1. In Figures 2 and 3, the specific parameters of the fairing and its transverse section can be seen.

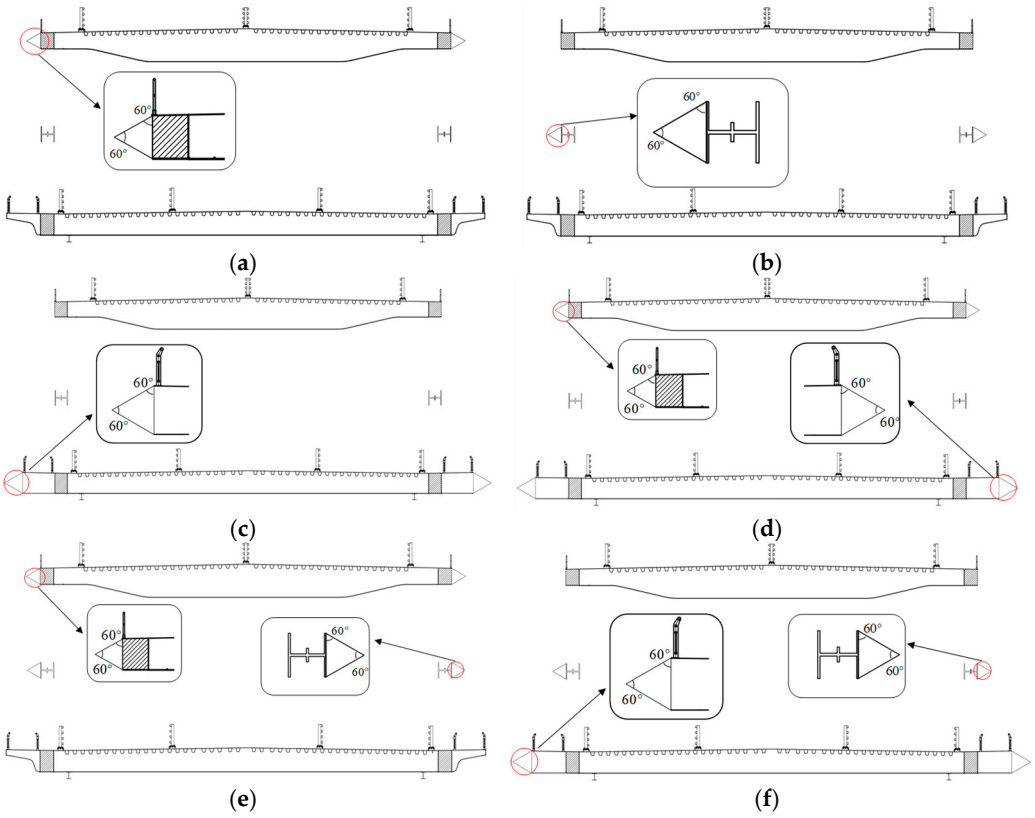


Figure 1. (**a**) Upper chord wind fairing; (**b**) web rod wind fairing; (**c**) lower chord wind fairing; (**d**) upper chord + lower chord wind fairing; (**e**) upper chord + web rod wind fairing; (**f**) web rod + lower chord wind fairing.

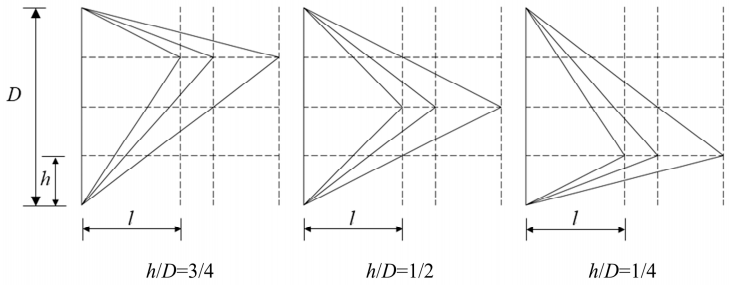


Figure 2. Nine types of wind fairing working conditions.

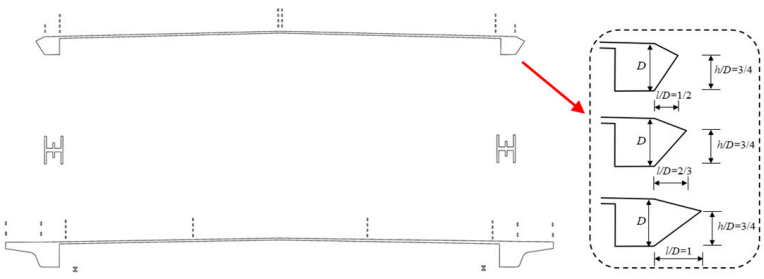


Figure 3. *Cont.*

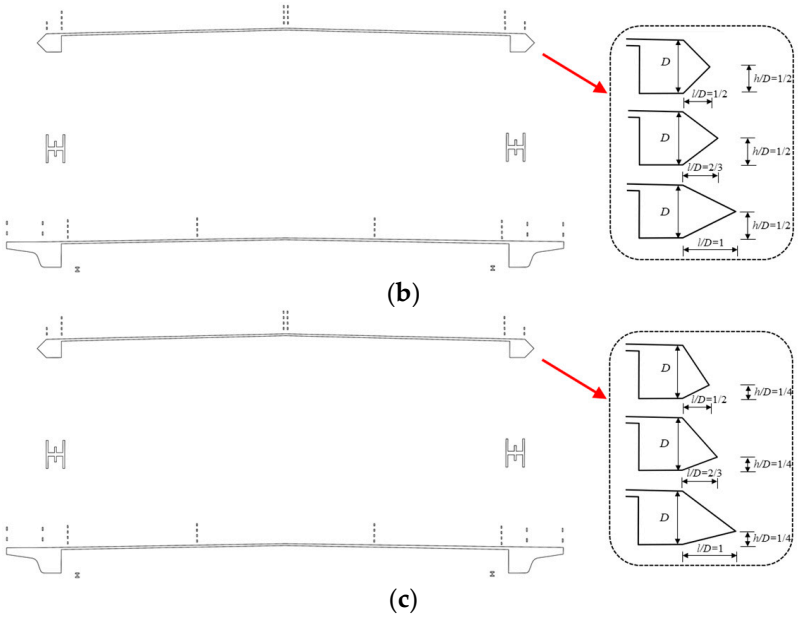


Figure 3. (**a**) $h/D = 3/4$; (**b**) $h/D = 1/2$; (**c**) $h/D = 1/4$.

2.2. VIV Evaluation Indicator

The setting of wind fairing measures changes the aerodynamic shape. Different cross-section aerodynamic shapes affect bridge VIV response, resulting in peak points of different heights in the VIV curve. To more intuitively evaluate the inhibition effect of different fairing parameters on VIV, we introduce parameter η to represent the inhibition effect of VIV. The expression of the VIV inhibition efficiency η is as follows:

$$\eta = \frac{y_0 - y_i}{y_0} \times 100\% \; or \; \eta = \frac{\theta_0 - \theta_i}{\theta_0} \times 100\% \tag{1}$$

In the formula, y_0 and θ_0 represent the maximum VIV amplitude of the original section, respectively, while y_i and θ_i represent the maximum VIV amplitude of the section with the set fairing, respectively. If η is positive, this indicates that the setting of the fairing has an inhibitory effect on VIV. If η is negative, this means that the setting of the fairing increases the VIV response. The larger the η, the better the fairing inhibition effect.

2.3. Aerodynamic Performance Optimization Process Based on Wind Fairing Parameters

By means of a wind tunnel test and numerical simulation, the optimization process of the aerodynamic shape of the main girder section with different fairing parameters as variables is shown in Figure 4. Firstly, a three-dimensional finite element model is established and its structural dynamic characteristics are calculated. The natural frequency, equivalent mass, vibration mode and other information are obtained. In accordance with this, the VIV test is designed, and the VIV response curves corresponding to different wind attack angles are obtained. In order to obtain the optimal position of the fairing, the vibration test is carried out under different working conditions with the position of the fairing as the variable, and the corresponding vibration inhibition efficiency is calculated. At the optimal fairing arrangement position, a variety of working conditions are further designed with different fairing size parameters for the numerical simulation. The vibration inhibition mechanism of the fairing is analyzed and the optimal fairing parameters are selected so as to obtain the optimal aerodynamic performance under fairing measures.

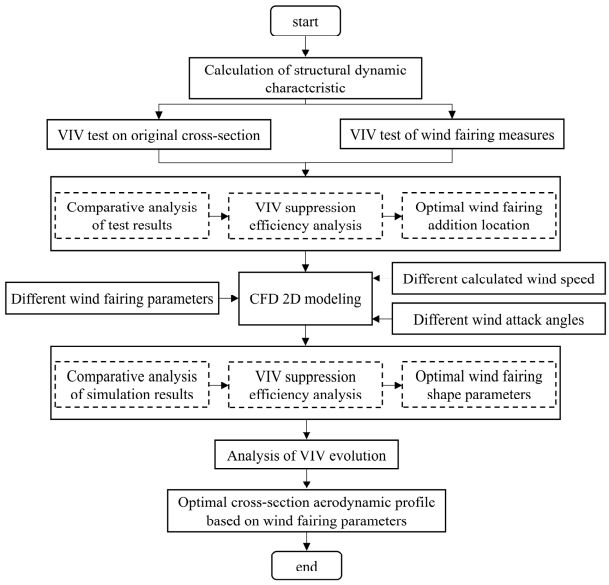


Figure 4. Aerodynamic shape optimization process for main girder section.

3. Calculation about Dynamic Characteristics of Bridge Structure

3.1. Simple Bridge Description

As the world's largest spanning highway–railway suspension bridge under construction [19], the Huangjuetuo Yangtze River Bridge is located in a subtropical humid monsoon climate zone and is greatly affected by the monsoon climate. The bridge is located in the Jiangbei District of Chongqing, China, and spans the Yangtze River. Due to the large span of the bridge and the harsh conditions of the wind on the river, the flow of the wind attack angle is easily affected. Therefore, it is particularly important to carry out wind resistance design. The bridge facade is shown in Figure 5. In addition to the web member, along the bridge axis, the transverse section of the bridge experiences almost no change. The bridge's typical transverse section can be seen in Figure 6.

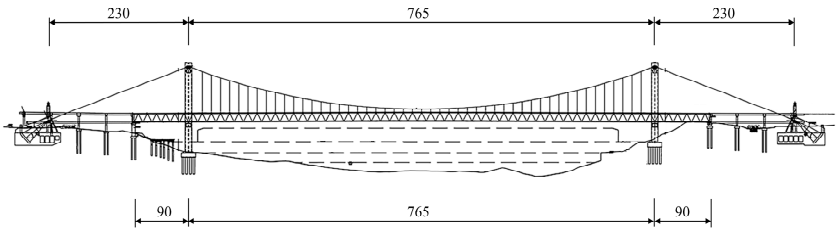


Figure 5. Bridge facade (unit: m).

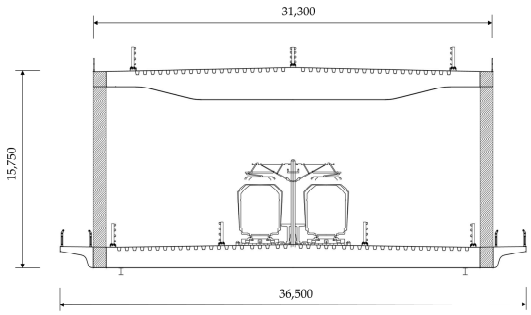


Figure 6. Bridge's typical transverse section (unit: mm).

3.2. Calculation of Structural Dynamic Characteristics

So as to ensure that the segment model can accurately simulate the vibration of the actual bridge under wind load, it is necessary to obtain accurate structural dynamic characteristics such as the natural frequency, equivalent mass and vibration mode of the bridge. Therefore, it is necessary to establish a three-dimensional finite element model that can fully reflect the dynamic effect of the structure. In Figure 7, the finite element model can be seen. For the benefit of clarifying the load and position of the loading point during the calculation, the stiffening girder is equivalent to 'single main girder' [20–23] by the principle of stiffness equivalence. The specific parameters of the main modes of the bridge are shown in Table 1, and the main modes are shown in Figure 8.

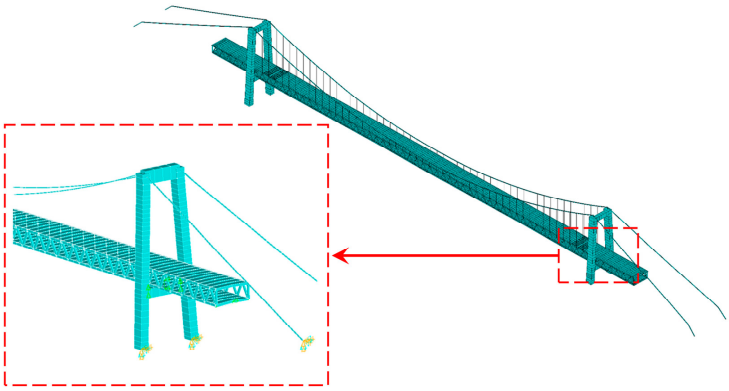
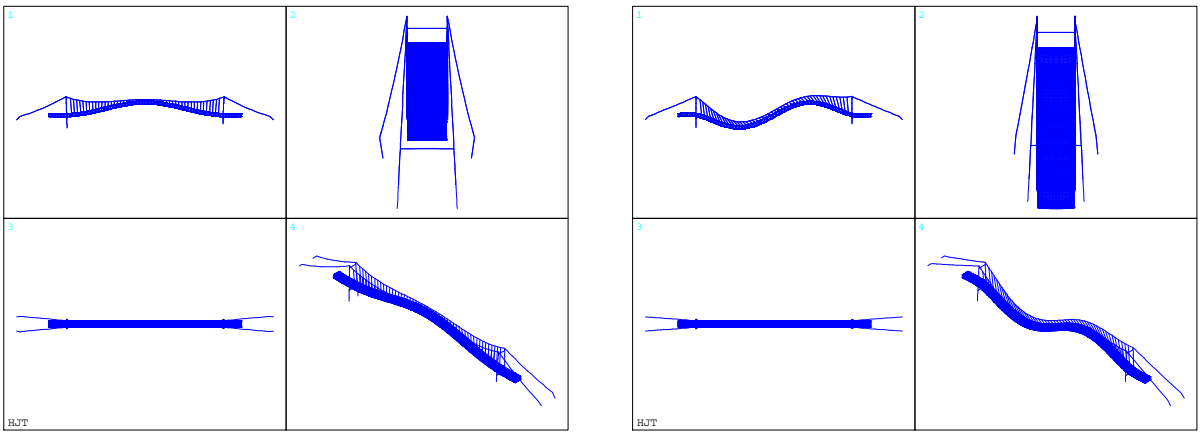


Figure 7. Finite element bridge model.

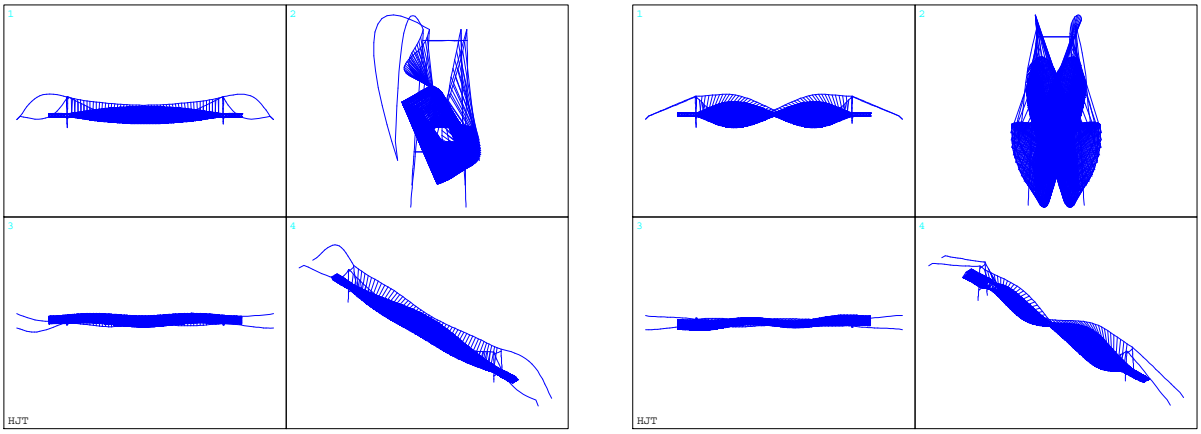
Table 1. Major mode parameters of bridge.

Order	Frequency	Mass	Moment of Inertia	Vibration Mode
3	0.2108 Hz	6.845×10^4 kg/m	/	first-order symmetric vertical bend
4	0.2368 Hz	7.008×10^4 kg/m	/	first-order objection vertical bend
11	0.4777 Hz	/	1.309×10^7 kg·m^2/m	first-order symmetric torsion
25	0.7055 Hz	/	1.228×10^7 kg·m^2/m	first-order objection torsion



(**a**) (**b**)

Figure 8. *Cont.*



(**c**) (**d**)

Figure 8. (**a**) First-order symmetric vertical bend; (**b**) first-order objection vertical bend; (**c**) first-order symmetric torsion; (**d**) first-order objection torsion.

4. Wind Tunnel Test of Main Girder Section with Wind Fairing Measures

After the preliminary preparation, the wind tunnel test is made in the DC wind tunnel laboratory of Chongqing University. This wind tunnel layout can be seen in Figure 9. It is 15 m long, 2.4 m wide, and 1.8 m high at the wind tunnel test section. In addition, the incoming flow in the wind tunnel laboratory is a uniform flow with low turbulence, and the wind speed adjustment range is 0.5 m/s~35 m/s, and turbulence, velocity field deviation, and other indicators meet the needs of this test.

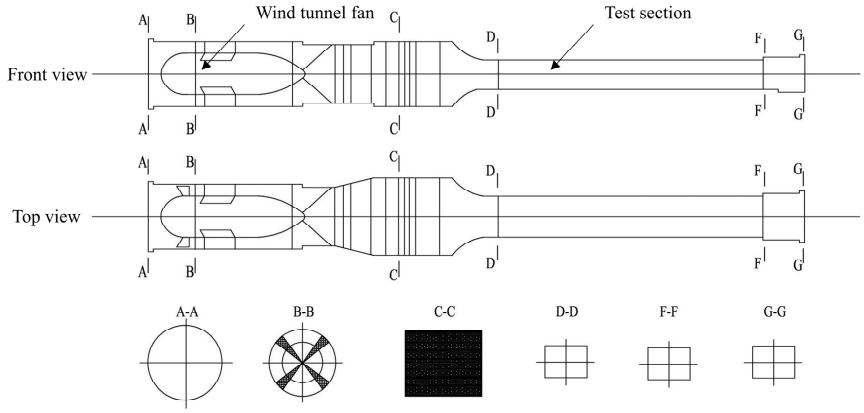


Figure 9. Wind tunnel layout.

4.1. Vortex-Induced Vibration Test of Original Section

Considering the laboratory conditions, segment model size and quality, the model scale ratio is selected as 1:55. In the VIV test, through the spring suspension system, the segment model can move vertically and rotate around the cross-section axis. A three-dimensional fluctuating wind speed measuring instrument is used to accurately measure the real-time wind speed of the flow field. A laser displacement sensor is used to measure and record the dynamic response of the bridge segment model. A slope measuring instrument is used to check the wind attack angle of the segment model. A high-frequency force balance is used to measure the three-component force of the segmental model. The specific test model is shown in Figure 10.

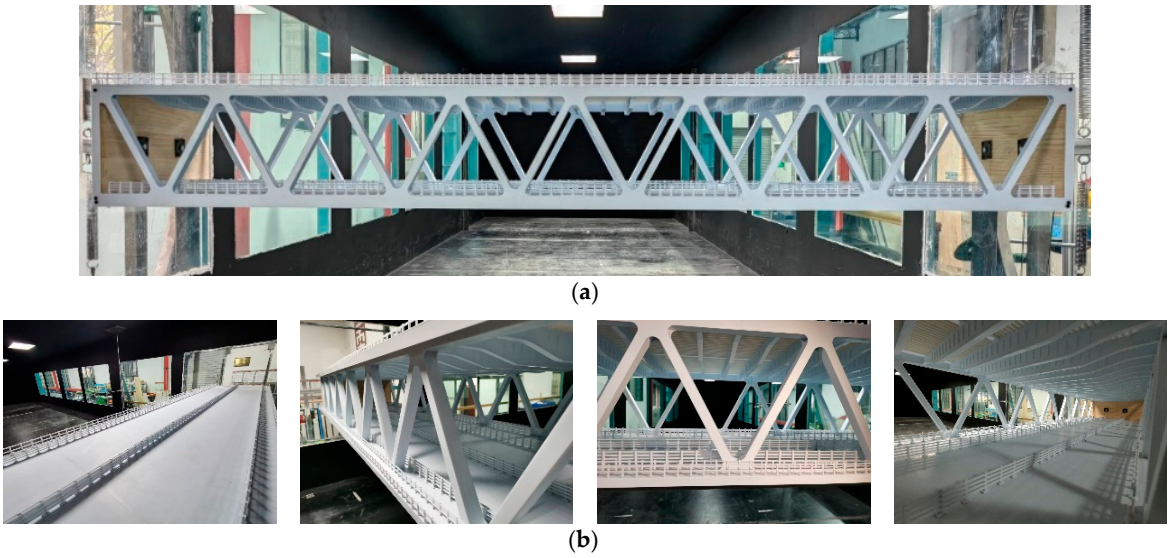


Figure 10. (**a**) Integral segment model; (**b**) local enlargement of the segment model.

The vibration test of the original cross-section model at five wind attack angles (α) of 0°, ±3°, and ±5° is carried out. The wind attack angle is the angle between the wind direction and the longitudinal axis of the bridge. The angle that increases lift is positive and the opposite is negative. The test wind speed is 0~10 m/s, and the corresponding real bridge wind speed is 0~44.8 m/s. The wind speed growth step is 0.08 m/s, and the corresponding wind speed of the real bridge is 0.36 m/s. When VIV may occur, the sampling frequency is encrypted, and the wind speed growth step is reduced to 0.04 m/s, corresponding to the actual bridge wind speed of 0.18 m/s. Each time, the displacement of model is recorded after the vibration is stable. The sampling time is 30 s, and the amplitude is the mean value of the vibration time history.

Through the vibration test, a variety of curves of VIV amplitude with the original section (C0) can be seen in Figure 11.

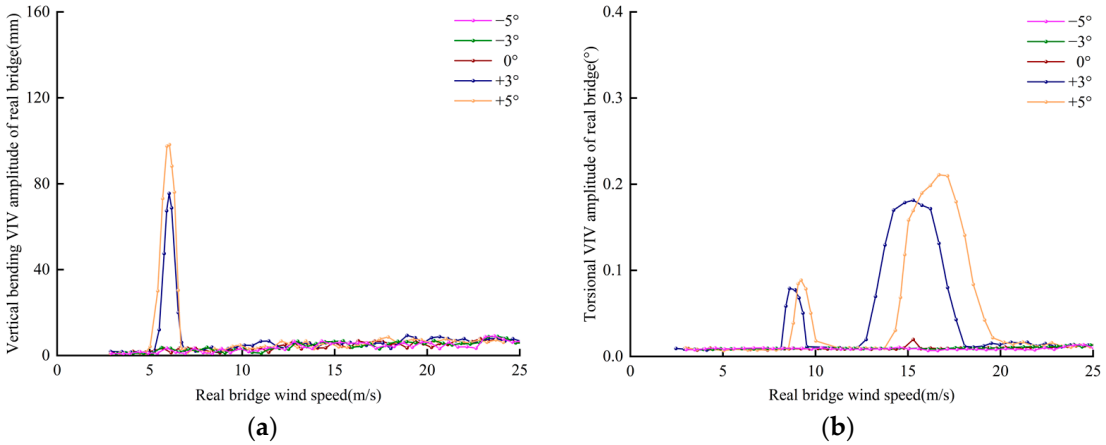


Figure 11. (**a**) Vertical bending VIV response; (**b**) torsional VIV response.

The specific test values are shown in Table 2. Compared with +3°, the maximum amplitudes of the vertical bending and torsional VIV increase significantly at +5°. The maximum amplitude of vertical bending VIV increased by 30.0%, while the maximum amplitude of torsional VIV at high air velocity and low air velocity increased by 16.6% and 12.7%, respectively. In addition, the onset air velocity of vertical bending VIV is slightly advanced, while its locking interval extent is evidently increased. The onset air velocity of torsional VIV is evidently delayed, while its locking interval extent is also slightly increased.

According to the test result, the wind attack angle plays a significant role in VIV response. The transverse section is more prone to VIV with a larger amplitude and longer locking range at a large attack angle.

Table 2. Major VIV modes of bridge.

α	VIV Type	Maximum Amplitude	Corresponding Real Speed	Frequency
+3°	Vertical bending	75.54 mm	6.05 m/s	2.227 Hz
	Torsional	0.079°, 0.181°	8.60 m/s, 15.28 m/s	4.289 Hz
+5°	Vertical bending	98.23 mm	6.06 m/s	2.227 Hz
	Torsional	0.089°, 0.211°	9.22 m/s, 16.67 m/s	4.289 Hz

4.2. Vortex-Induced Vibration Test of Cross-Section with Wind Fairing Measures

The 60° equilateral triangle fairing is selected as the research object, and the influence of the fairing's location on the VIV response is studied. According to the inhibition efficiency of VIV under various conditions, the optimal location of the fairing on the main girder section is obtained. The wind attack angle is set to +3° and +5°, and the test air velocity range is 0~10 m/s. According to the specific test conditions, the fairing test model is set as shown in Figure 12.

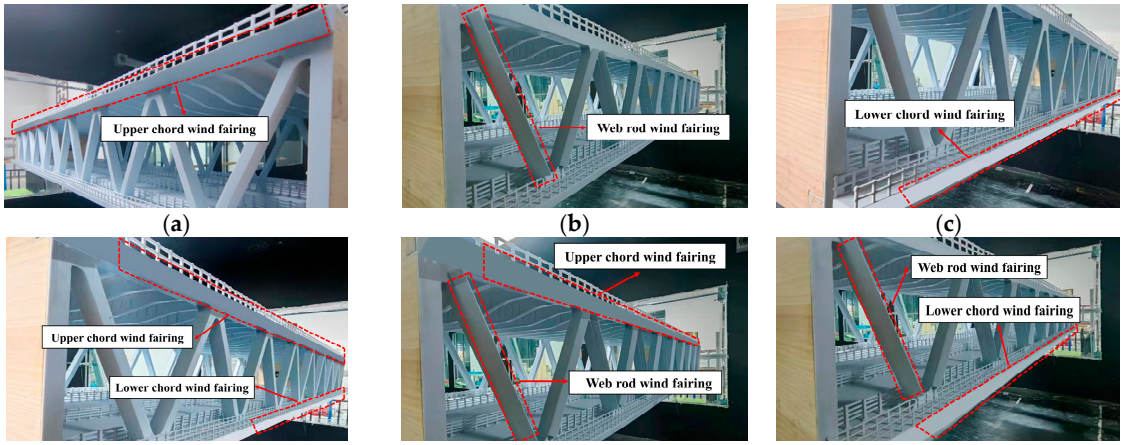


Figure 12. (**a**) C1; (**b**) C2; (**c**) C3; (**d**) C4; (**e**) C5; (**f**) C6.

Through the VIV inhibition test of the wind fairing, various VIV curves of six working conditions under two angles are obtained, as shown in Figures 13 and 14, separately (the wind speed and amplitude are transformed into real bridge values).

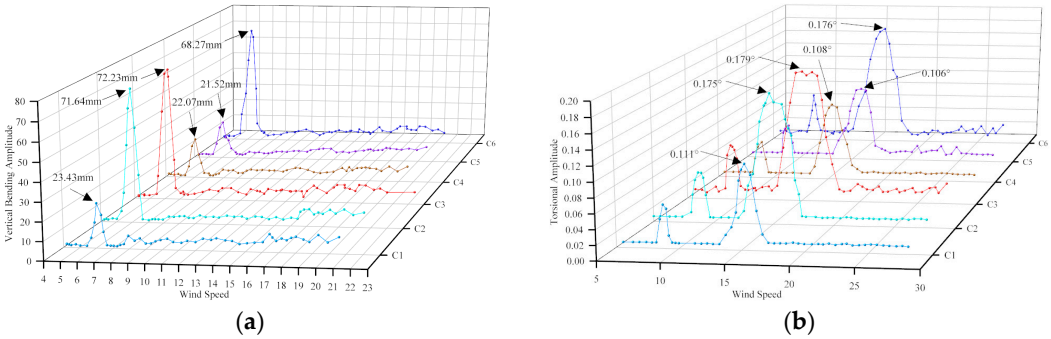
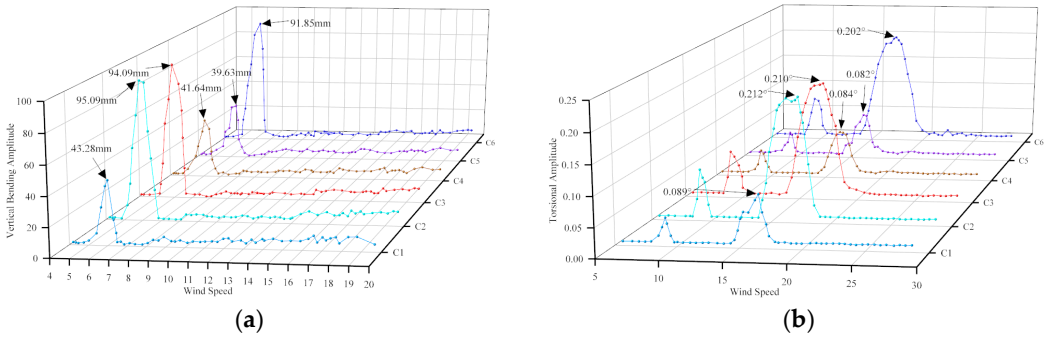


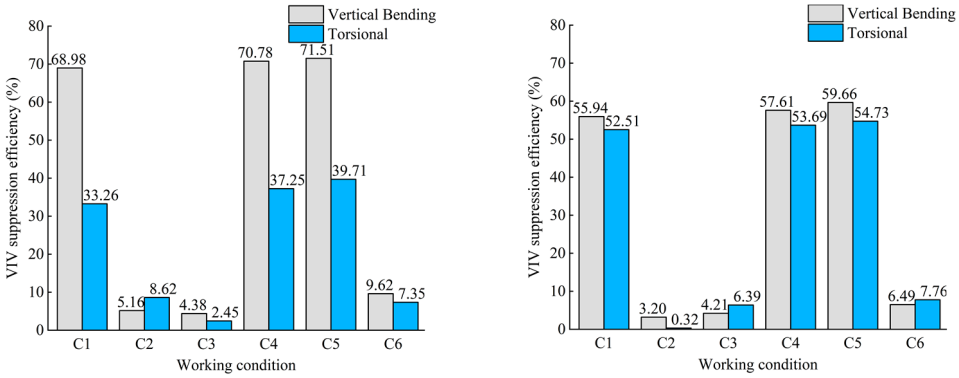
Figure 13. (**a**) Vertical bending VIV at +3°; (**b**) torsional VIV at +3°.



(**a**) (**b**)

Figure 14. (**a**) Vertical bending VIV at +5°; (**b**) torsional VIV at +5°.

The VIV inhibition efficiency is shown in Figure 15 (the inhibition efficiency of torsional VIV is the average of the inhibition efficiency of the main and minor locking intervals).



(**a**) (**b**)

Figure 15. (**a**) VIV inhibition efficiency at +3°; (**b**) VIV inhibition efficiency at +5°.

Upon conducting a comprehensive comparison of the six fairing conditions, it can be seen that the influence of the fairing measures on the vibration inhibition of the vertical bending VIV is much greater than the influence on the torsional VIV. The highest inhibition efficiency of vertical bending VIV is 71.51%, the lowest is 3.20%, and the average is 34.80%. The highest inhibition efficiency of torsional VIV is 54.73%, the lowest is 0.32%, and the average is 25.34%. C1, C4, and C5 conditions are able to efficiently inhibit vertical bending and torsional VIV responses, but compared with the C1 condition, the VIV inhibition efficiency on the C4 and C5 conditions is not significantly improved. Therefore, the C1 working condition is the optimal working condition, that is, the upper chord is the optimal fairing addition position. The average inhibition efficiency of vertical bending VIV at two angles is 62.46%, and the average inhibition efficiency of torsional VIV is 42.89%. Regarding the vertical bending VIV, it is speculated that the vortex zone of the upper board dominates.

5. Influence of Wind Fairing Parameters on Vortex-Induced Vibration

For the benefit of finding out optimal wind fairing parameters, based on the optimal position of the fairing (upper chord), the vertical bending VIV response as well as the fairing influence mechanism on the main girder under different parameters are studied by means of numerical simulation.

5.1. Establishment of 2D CFD Model

The CFD geometric model uses the same scale ratio as the test model. The geometric model of main girder cross-section with wind fairing measures can be seen in Figure 16.

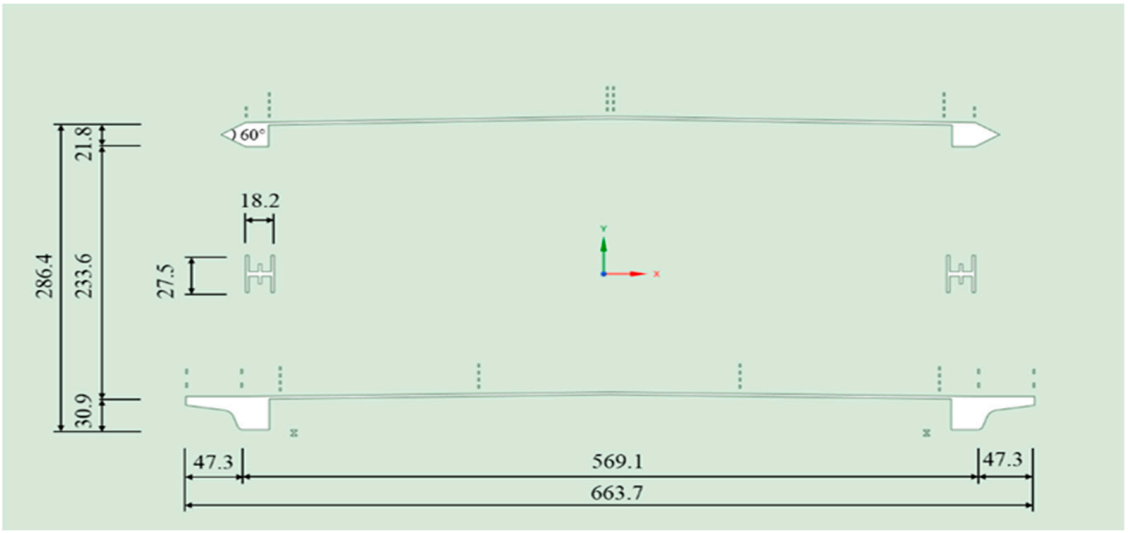


Figure 16. Geometric model of the main girder section setting fairing.

This numerical simulation domain is composed of a near-wall rigid motion region + a dynamic grid region + a background grid region. According to Figure 17, boundary conditions are strictly set. The turbulence model uses an SST *k*-*ω* model. The model blocking rate in the calculation region is 0.5%. It meets the permitted model requirement of 5% [24,25].

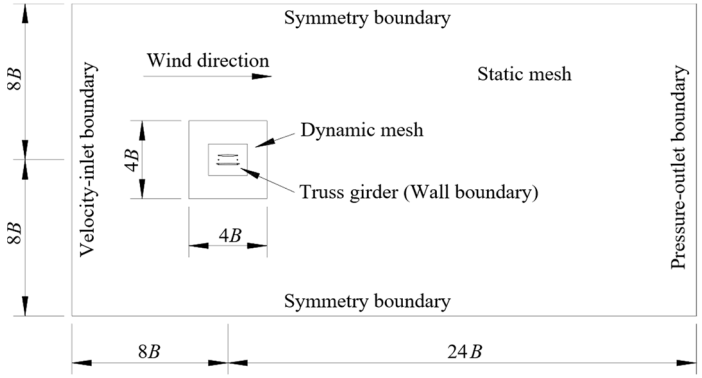


Figure 17. Calculation domain dimension and boundary condition setting.

Reasonable meshing is the key to the success of a numerical simulation [26]. The total number of grids of the two-dimensional section model generated in the simulation is about 78.5×10^4, and the specific grid division is shown in Figure 18.

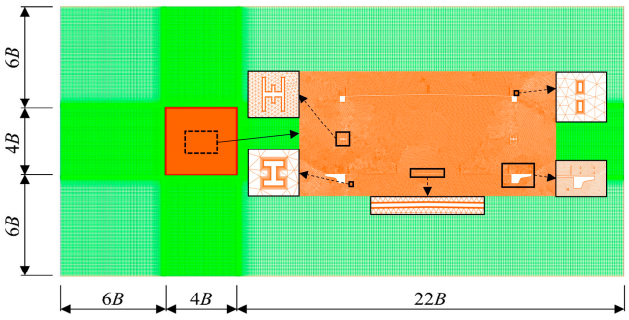


Figure 18. Mesh division of calculation domain.

5.2. Irrelevant Verification

For the purpose of ensuring the veracity of the CFD calculation outcome, the computational time step, the mesh quantity and the position independence of the web member are verified for the original two-dimensional model [27–32].

(1) Time step independence verification

Five time steps of 1×10^{-3} s, 5×10^{-4} s, 1×10^{-4} s, 5×10^{-5} s, and 1×10^{-5} s are used to calculate the drag, lift, and torque coefficients (C_D, C_L, and C_M) of the model at +3° and 10.0 m/s real bridge wind speed. The independence of the time step is verified by the average value ($\overline{C}$) and standard deviation (σ) of the three-force coefficient [33–37]. The specific results are shown in Table 3.

Table 3. Time step independence verification calculation results.

Computational Time Step (s)		0.001	0.0005	0.0001	0.00005	0.00001
mean value	$\overline{C_D}$	0.6741	0.6954	0.7221	0.7232	0.7250
	$\overline{C_L}$	0.8137	0.8254	0.8456	0.8451	0.8501
	$\overline{C_M}$	0.0181	0.0198	0.0285	0.0289	0.0290
root mean square error	σ_D	0.0345	0.0352	0.0205	0.0201	0.0174
	σ_L	0.0754	0.0711	0.0458	0.0421	0.0418
	σ_M	0.0222	0.0187	0.0119	0.0118	0.0125

The mean and standard deviation of 1×10^{-3} and 5×10^{-4} are significantly higher than those of the other three groups. On the basis of 1×10^{-4}, the time step is further reduced, and the calculation results have no significant change. Therefore, in the numerical simulation, the time step is 1×10^{-4} s, the calculation step is 1×10^5 steps, and the total calculation time is 10 s.

(2) Grid number independence verification

Four grid numbers of 39.3×10^4, 78.5×10^4, 98.0×10^4 and 117.6×10^4 are selected to calculate the three-force coefficients of the model under +3° and 10.0 m/s real bridge wind speed, and the independence of the grid number is verified. The specific results are shown in Table 4.

Table 4. Mesh number independence verification calculation results.

Mesh Number ($\times 10^4$)		39.3	78.5	98.0	117.6
y+		0.1215	0.0751	0.0749	0.0742
average value	$\overline{C_D}$	0.7091	0.7221	0.7243	0.7265
	$\overline{C_L}$	0.8217	0.8456	0.8502	0.8514
	$\overline{C_M}$	0.0219	0.0285	0.0288	0.0290
standard deviation	σ_D	0.0421	0.0205	0.0265	0.0224
	σ_L	0.0945	0.0458	0.0471	0.0431
	σ_M	0.0391	0.0119	0.0108	0.0134

On the basis of 78.5×10^4 grids, the number of grids is further increased, and the calculation results have no significant change. Increasing the number of grids improves the calculation accuracy but greatly increases the amount of calculation, so the number of grids for the numerical simulation is controlled at about 78.5×10^4.

(3) The position independence of the web member section verification

The three cross-sections of F1, F2, and F3 are intercepted, and the three-force coefficients of the model at +3° and 10.0 m/s real bridge wind speed are calculated, respectively, and the independence of the web member is verified by $\overline{C}$ and σ. The transverse sections of F1, F2, and F3 are shown in Figure 19, where d is the interval from the web member core to the upper chord core. These verification results of irrelevance are shown in Table 5.

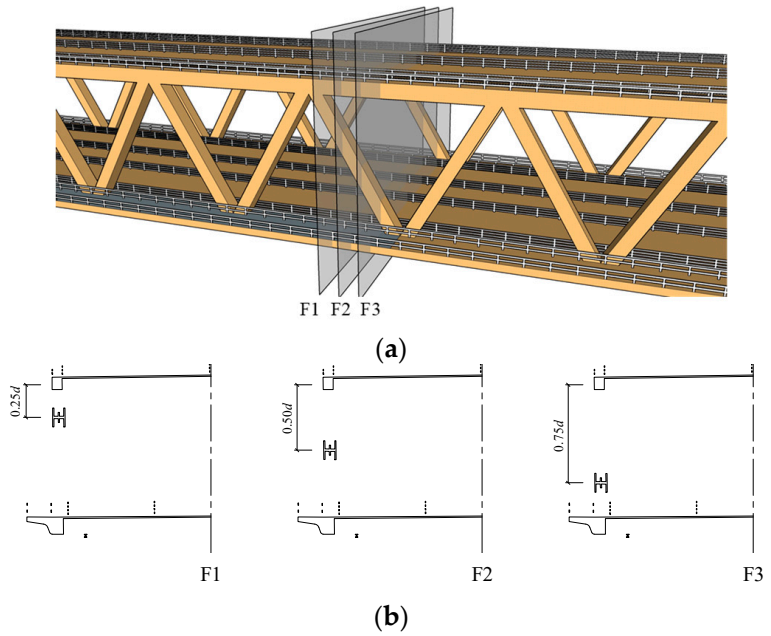


Figure 19. (**a**) Schematic representation of cross-section selection; (**b**) half-section of main girder.

Table 5. Web position independence verification calculation results.

Cross-Section Number		F1	F2	F3
average value	$\overline{C_D}$	0.7186	0.7221	0.7255
	$\overline{C_L}$	0.8245	0.8456	0.8512
	$\overline{C_M}$	0.0279	0.0285	0.0291
standard deviation	σ_D	0.0212	0.0205	0.0198
	σ_L	0.0525	0.0458	0.0478
	σ_M	0.0103	0.0119	0.0133

The difference in the static three-force coefficients under the three web sections obtained by numerical simulation is within 5%. Therefore, the F2 transverse section is selected in the numerical simulation.

5.3. Simulation of Vortex-Induced Vibration under Different Wind Fairing Parameters

In order to explore the optimal shape parameters of the fairing, 18 different wind speeds, two different wind attack angles, and nine different cross-section parameters of the fairing are numerically simulated. The wind speed range is 1.00~1.68 m/s, and the wind speed step is 0.04 m/s at +3° and +5°.

Through numerical simulation, various curves of different working conditions are obtained as shown in Figure 20. The corresponding vibration inhibition efficiency of wind fairing conditions is shown in Table 6.

From the overall working conditions, when the ratio of h to D is fixed, the greater the ratio of l to D, the higher the vertical bending VIV inhibition efficiency. On the contrary, when the ratio of l to D is fixed, the larger the ratio of h to D, the lower the vertical bending VIV inhibition efficiency is. The VIV inhibition efficiency at +3° is higher than that at +5°. The VIV inhibition efficiency of D9 is the highest, with an average of 63.01%. The VIV inhibition efficiency of D3 is the lowest, with an average of 34.16%.

To explore the mechanism of a wind fairing to inhibit VIV, these upper board stream area changes at the original section and the F3 cross-section at +5° are analyzed as seen in Figure 21.

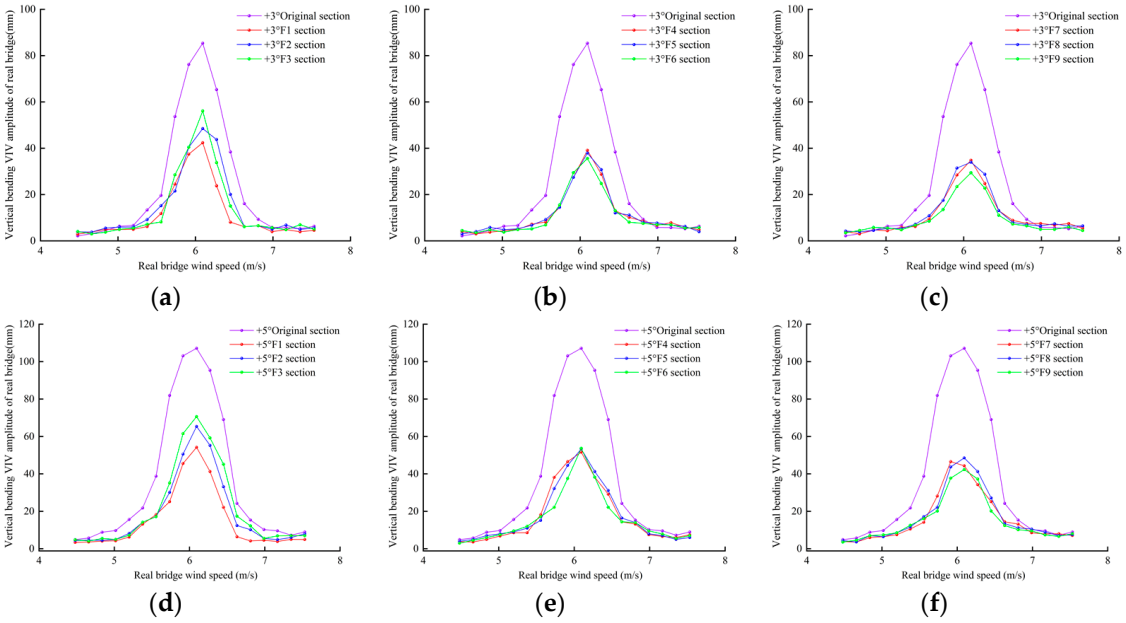


Figure 20. (**a**) $h/D = 3/4$, $\alpha = +3°$; (**b**) $h/D = 1/2$, $\alpha = +3°$; (**c**) $h/D = 1/4$, $\alpha = +3°$; (**d**) $h/D = 3/4$, $\alpha = +5°$; (**e**) $h/D = 1/2$, $\alpha = +5°$; (**f**) $h/D = 1/4$, $\alpha = +5°$.

Table 6. Wind fairing simulation results.

Section Number	Maximum Vertical Bending VIV Amplitude (+3°/+5°)	η
Original section	85.36 mm/107.14 mm	/
F1 section	42.38 mm/54.22 mm	50.35%/49.39%
F2 section	48.52 mm/65.37 mm	43.16%/38.99%
F3 section	56.13 mm/70.64 mm	34.24%/34.07%
F4 section	39.13 mm/51.62 mm	54.16%/51.92%
F5 section	37.93 mm/53.34 mm	55.56%/50.21%
F6 section	35.61 mm/53.71 mm	58.28%/49.87%
F7 section	34.83 mm/46.52 mm	59.20%/56.28%
F8 section	33.98 mm/48.53 mm	60.19%/57.70%
F9 section	29.44 mm/42.32 mm	65.51%/60.50%

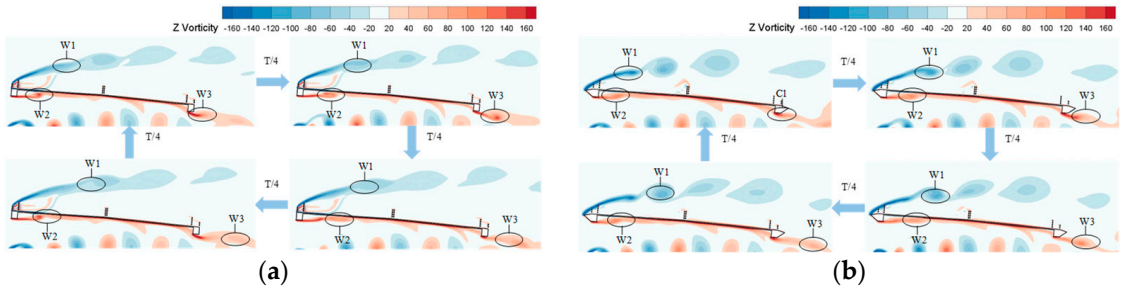


Figure 21. (**a**) Original section; (**b**) F3 section.

Compared with the original section, the first separation point of this air stream in the F3 section moves forward to the tip of the wind fairing. Subsequently, the airflow is rectified by the fairing during the flow to the upper bridge board, thereby significantly reducing the energy of the shear layer. The upper airflow is attached to the upper surface of the fairing, and a small part of the shunt is dispersed into a small-sized vortex after cross over the anti-collision railing slit, while most of the shunt occurs via the secondary separation on the upper side of the railing, resulting in a smaller W1 vortex than the original section scale. Meanwhile, this lower-side airflow produces vortex separation along the lower surface of

the fairing. Not only the scale but also the vorticity of W2 vortex are significantly reduced comparable to the original cross-section, and airflow as well as the attachment point on the lower side of the upper bridge board are significantly moved backward compared to the original cross-section. Airflow moves slowly along the lower side of the upper bridge board to the leeward side. Accompanying this, it produces a W3 vortex which is basically as same as the original section scale but has a lower vorticity. Although this wind fairing does not change the vortex shedding forms of the original section, it changes the first separation point of the airflow, as well as movement direction, so that the vortex scale generated by the airflow is smaller and the vorticity is lower, thus effectively suppressing the VIV.

6. Conclusions

Making Huangjuetuo Yangtze River Bridge a research target, the VIV performance of the main girder section with wind fairing measures is tested by the section model wind tunnel test, and the optimal fairing arrangement position is found. Combined with CFD numerical simulation, the vibration inhibition efficiency and influence mechanism of different fairing parameters on VIV are analyzed, and the influence of fairing parameters on the aerodynamic performance of the long-span double-deck steel truss suspension bridge is realized. From the aspects of VIV response and flow field distribution, the following conclusions are drawn:

(1) Through the wind tunnel test, at +3° and +5° wind attack angles, with the addition of wind speed, at the original section of the main girder, what first occurs is the vertical bending VIV, then two torsional VIV with different maximum amplitudes occur, and the peak value of VIV at +5° is higher than that at +3°.

(2) By the VIV test, how impact affects the wind fairing position on VIV is studied. The upper chord is determined to be the optimal position of the fairing. Under two wind attack angle conditions, the average inhibition efficiency of vertical bending VIV is 62.46%, while the average inhibition efficiency of torsional VIV is 42.89%. It can be seen that the inhibition effect of the fairing on vertical bending VIV is greater than that of torsional VIV. Among them, the maximum inhibition efficiency of vertical bending VIV is 71.51%, the minimum is 3.20%, and the average is 34.80%. The highest inhibition efficiency of torsional VIV is 54.73%, the lowest is 0.32%, and the average is 25.34%.

(3) Based on the optimal position of the wind fairing, the height, D, of the truss section is taken as the quantitative value, and the horizontal size, l, of the fairing and the relative height, h, of the fairing are taken as the variables. A total of nine kinds of fairing conditions are set up for numerical simulation. When $h/D = 1/4$ and $l/D = 1$, the optimal fairing parameters are attained. From the airflow field distribution, these vortex zones around the upper board dominate vertical bending VIV. Therefore, the upper chord fairing weakens the energy of the shear layer by advancing the airflow separation point, breaking the vortex and reducing the vortex size to suppress VIV so as to achieve the purpose of optimizing the aerodynamic performance of the main girder.

Author Contributions: Conceptualization, G.Y. and Y.Y.; methodology, G.Y. and Y.Y.; software, L.L.; validation, Y.Y.; formal analysis, L.L.; writing—original draft preparation, L.L., B.W., D.W., H.Y. and H.Q.; writing—review and editing, G.Y. and Y.Y.; visualization, L.L.; supervision, G.Y.; funding acquisition, G.Y. and Y.Y. All authors have read and agreed to the published version of the manuscript.

Funding: This research was funded by National Natural Science Foundation of China (52108435), Central Universities' Basic Research Operating Expenses (2023CDJXY-031) and Chongqing Urban Rail Express Line Full Life Cycle CIM Technology Application Research and Demonstration Research Project (S20220413).

Data Availability Statement: The data presented in this study are available on request from the corresponding author.

Acknowledgments: The authors thanks the Innovation and Talent Recruitment Base of High-performance Wind Energy System and the Effective Operation of Wind Farms in Chongqing University and the Chongqing Key Laboratory of Wind Engineering and Wind Energy Utilization in Chongqing University.

Conflicts of Interest: Authors Dawu Wang, Hui Yu, and Hao Qu were employed by the company Chongqing Railway Group Co., Ltd. The remaining authors declare that the research was conducted in the absence of any commercial or financial relationships that could be construed as a potential conflict of interest.

References

1. Gang, Y.; Yang, Y.; Wu, B.; Liu, L.; Zhang, L.-L. Aerodynamic admittance influence on buffeting performance of suspension bridge with streamlined deck. *J. Vibroengineering* **2019**, *21*, 198–214. [CrossRef]
2. Wu, B.; Zhou, J.; Li, S.; Xin, J.; Zhang, H.; Yang, X. Combining active and passive wind tunnel tests to determine the aerodynamic admittances of a bridge girder. *J. Wind. Eng. Ind. Aerodyn.* **2022**, *231*, 105180. [CrossRef]
3. Zhao, L.; Cui, W.; Shen, X.; Xu, S.; Ding, Y.; Ge, Y. A fast on-site measure-analyze-suppress response to control vortex-induced-vibration of a long-span bridge. *Structures* **2022**, *35*, 192–201. [CrossRef]
4. Yang, Y.; Zhang, J.; Cao, F.; Ge, Y.; Zhao, L. Evaluation and improvement of wind environment and vehicle safety on long-span bridge deck under strong crosswind. *J. Wind Eng. Ind. Aerodyn.* **2022**, *228*, 105089. [CrossRef]
5. Ge, Y.; Zhao, L.; Cao, J. Case study of vortex-induced vibration and mitigation mechanism for a long-span suspension bridge. *J. Wind Eng. Ind. Aerodyn.* **2022**, *220*, 104866. [CrossRef]
6. Xiao, H.; Liu, Z.; Chen, Z.; Liu, Z.; Yan, A.; Yang, O. Experimental and numerical study on vibration response, VIV mechanism and aerostatic coefficients of triple-separated decks under different vertical distances. *J. Wind Eng. Ind. Aerodyn.* **2024**, *250*, 105782. [CrossRef]
7. He, M.; Liang, P.; Zhang, Y.; Wang, Y.; Wang, K. Identification, tracking and warning of vortex induced vibration using k-means clustering method. *Struct. Infrastruct. Eng.* **2022**, *20*, 380–393. [CrossRef]
8. Kim, S.-J.; Shim, J.-H.; Kim, H.-K. How wind affects vehicles crossing a double-deck suspension bridge. *J. Wind Eng. Ind. Aerodyn.* **2020**, *206*, 104329. [CrossRef]
9. He, X.-H.; Li, H. Review of aerodynamics of high-speed train-bridge system in crosswinds. *J. Cent. South Univ.* **2020**, *27*, 1054–1073. [CrossRef]
10. Xu, Z.; Wang, H.; Xing, C.; Tao, T.; Mao, J.; Liu, Y. Physics guided wavelet convolutional neural network for wind-induced vibration modeling with application to structural dynamic reliability analysis. *Eng. Struct.* **2023**, *297*, 117027. [CrossRef]
11. Irwin, P.A. Bluff body aerodynamics in wind engineering. *J. Wind Eng. Ind. Aerodyn.* **2008**, *96*, 701–712. [CrossRef]
12. Bruno, L.; Coste, N.; Fransos, D. Simulated flow around a rectangular 5:1 cylinder: Spanwise discretisation effects and emerging flow features. *J. Wind Eng. Ind. Aerodyn.* **2012**, *104–106*, 203–215. [CrossRef]
13. Bruno, L.; Salvetti, M.V.; Ricciardelli, F. Benchmark on the Aerodynamics of a Rectangular 5:1 Cylinder: An overview after the first four years of activity. *J. Wind Eng. Ind. Aerodyn.* **2014**, *126*, 87–106. [CrossRef]
14. Zhong, Y.; Li, M.; Ma, C. Aerodynamic admittance of truss girder in homogenous turbulence. *J. Wind Eng. Ind. Aerodyn.* **2018**, *172*, 152–163. [CrossRef]
15. Yao, G.; Wu, L.; Yang, Y.; Liu, M.; Chen, Y.; Du, H. Study on the Suppression Effect on Vortex-Induced Vibration of Double-Deck Truss Girder by the Spatial Position of the Deflector Plate. *Appl. Sci.* **2023**, *13*, 9764. [CrossRef]
16. Yao, G.; Chen, Y.; Yang, Y.; Zheng, Y.; Wu, L.; Du, H. Research on Mechanism of Vortex-Induced Vibration Railing Effect of Double-Deck Large-Span Suspension Bridge. *Appl. Sci.* **2023**, *13*, 9314. [CrossRef]
17. Bai, H.; Li, R.; Xu, G.; Kareem, A. Aerodynamic performance of Π-shaped composite deck cable-stayed bridges including VIV mitigation measures. *J. Wind Eng. Ind. Aerodyn.* **2021**, *208*, 104451. [CrossRef]
18. Li, Y.; Chen, X.; Yu, C.; Togbenou, K.; Wang, B.; Zhu, L. Effects of wind fairing angle on aerodynamic characteristics and dynamic responses of a streamlined trapezoidal box girder. *J. Wind Eng. Ind. Aerodyn.* **2018**. [CrossRef]
19. Yao, G.; Chen, Y.; Yang, Y.; Zheng, Y.; Du, H.; Wu, L. Investigation of Vortex-Induced Vibration of Double-Deck Truss Girder with Aerodynamic Mitigation Measures. *J. Mar. Sci. Eng.* **2023**, *11*, 1118. [CrossRef]
20. Li, P.; Wang, H. A novel strategy for the crossarm length optimization of PSSCs based on multi-dimensional global optimization algorithms. *Eng. Struct.* **2021**, *238*, 112238. [CrossRef]
21. Li, P.; Chen, G.; Qiu, J.; Qian, J.; Ding, D.; Jian, B.; Zhang, X.; Xiong, G. Experimental and numerical investigation into the load-carrying capacity of aluminium alloy H-sectional stocky columns under axial compression. *J. Build. Eng.* **2024**, *87*, 108777. [CrossRef]
22. Chen, X.; Zhu, C.; Ma, C.; Li, Q. Vortex-induced vibration of twin-box girder and its aerodynamic characteristics study based on high-order dynamic decomposition. *J. Wind Eng. Ind. Aerodyn.* **2024**, *249*, 105719. [CrossRef]
23. Zhao, C.-X.; Liu, J.-N.; Li, B.-Q.; Ren, D.; Chen, X.; Yu, J.; Zhang, Q. Multiscale Construction of Bifunctional Electrocatalysts for Long-Lifespan Rechargeable Zinc–Air Batteries. *Adv. Funct. Mater.* **2020**, *30*, 2003619. [CrossRef]

24. Khosravi, M.; Mosaddeghi, F.; Oveisi, M.; khodayari-b, A. Aerodynamic drag reduction of heavy vehicles using append devices by CFD analysis. *J. Cent. South Univ.* **2015**, *22*, 4645–4652. [CrossRef]
25. Wang, C.; Hua, X.; Huang, Z.; Tang, Y.; Chen, Z. Post-critical behavior of galloping for main cables of suspension bridges in construction phases. *J. Fluids Struct.* **2021**, *101*, 103205. [CrossRef]
26. Sarwar, M.W.; Ishihara, T. Numerical study on suppression of vortex-induced vibrations of box girder bridge section by aerodynamic countermeasures. *J. Wind Eng. Ind. Aerodyn.* **2010**, *98*, 701–711. [CrossRef]
27. Xiao, H.; Liu, Z.; He, F.; Chen, Z.; Liu, Z.; Yan, A. Aerodynamic Interference Effects on Vortex-Induced Vibration of Two Parallel Railway– and Highway–Cable-Stayed Bridges with Triple-Separated Decks. *J. Bridge Eng.* **2024**, *29*, 04023112. [CrossRef]
28. Haohong, L.; Liang, L.Z.; Bo, W. Effects of the angle of attack on the aerodynamic characteristics of a streamlined box girder. *Adv. Struct. Eng.* **2021**, *24*, 2090–2104. [CrossRef]
29. Lei, W.; Wang, Q.; Zhang, Y.; Li, Z. Study on VIV performance of streamlined steel box girder of a sea-crossing cable-stayed bridge. *Ocean Eng.* **2024**, *295*, 116897. [CrossRef]
30. Hu, C.; Zhao, L.; Wang, X.; Ge, Y. Spatio-temporal distribution of aerodynamic forces and their associated vortex drift patterns around a closed-box girder during torsional vortex-induced vibration. *Eng. Struct.* **2024**, *302*, 117459. [CrossRef]
31. Sun, H.; Zhu, L.-D.; Tan, Z.-X.; Zhu, Q.; Meng, X.-L. Spanwise layout optimization of aerodynamic countermeasures for multi-mode vortex-induced vibration control on long-span bridges. *J. Wind Eng. Ind. Aerodyn.* **2024**, *244*, 105616. [CrossRef]
32. Liu, Z.; He, F.; Yan, A.; Liu, Z.; Yin, T.; Chen, Z. Mechanism and Aerodynamic Countermeasures of Vortex-Induced Vibration of a Cable-Stayed Bridge with Narrow ΠΙ-Shaped Girder Sections. *J. Bridge Eng.* **2023**, *28*, 04023090. [CrossRef]
33. He, H.; Wang, J.; Wang, F. Investigation of the Effects of Vortex Isolation Plates with Different Opening Ratios and Sizes on Vortex-Induced Vibration. *Appl. Sci.* **2024**, *14*, 3863. [CrossRef]
34. Wang, C.; Huang, Z.; Hua, X.; He, X.; Zhou, S.; Chen, Z. Aerodynamic mechanism of triggering and suppression of vortex-induced vibrations for a triple-box girder. *J. Wind Eng. Ind. Aerodyn.* **2022**, *227*, 105051. [CrossRef]
35. Guo, S.; Jiang, Y.; Zhang, W.; Zeng, Y. Study on Dynamic Characteristics of Long-Span Highway-Rail Double-Tower Cable-Stayed Bridge. *Buildings* **2024**, *14*, 1733. [CrossRef]
36. Wang, Y.; Feng, H.; Xu, N.; Zhong, J.; Wang, Z.; Yao, W.; Jiang, Y.; Laima, S. A Data-Driven Model for Predictive Modeling of Vortex-Induced Vibrations of a Long-Span Bridge. *Appl. Sci.* **2024**, *14*, 2233. [CrossRef]
37. Zhang, Y.-M.; Wang, H.; Bai, Y.; Mao, J.-X.; Chang, X.-Y.; Wang, L.-B. Switching Bayesian dynamic linear model for condition assessment of bridge expansion joints using structural health monitoring data. *Mech. Syst. Signal Process.* **2021**, *160*, 107879. [CrossRef]

Disclaimer/Publisher's Note: The statements, opinions and data contained in all publications are solely those of the individual author(s) and contributor(s) and not of MDPI and/or the editor(s). MDPI and/or the editor(s) disclaim responsibility for any injury to people or property resulting from any ideas, methods, instructions or products referred to in the content.